PAPER

Sunlight driven photocatalytic degradation of organic pollutants using a MnV$_2$O$_6$/BiVO$_4$ heterojunction: mechanistic perception and degradation pathways†

Karina Bano,[a] Susheel K. Mittal,[b] Prit Pal Singh [iD] *[a] and Sandeep Kaushal [iD] *[a]

In the field of photocatalysis, fabrication of a heterojunction structure with effective charge separation at the interface and charge shift to enhance the photocatalytic activity has acquired extensive consideration. In the present investigation, MnV$_2$O$_6$/BiVO$_4$ heterojunction samples with excellent photocatalytic performance under sunlight irradiation were conveniently synthesized by a hydrothermal technique, and characterized by UV-Vis, FTIR, XRD, FESEM, HRTEM, PL, BET and XPS techniques. The prepared samples were investigated as photocatalysts for degrading MB and RhB dyes under sunlight. Among various samples of MnV$_2$O$_6$/BiVO$_4$, the S-V hetero-junction sample exhibited maximum photocatalytic activity with 98% and 96% degradation of MB and RhB dyes, respectively, in 6 and 35 min. The high photocatalytic activity of MnV$_2$O$_6$/BiVO$_4$ may be due to the successful generation and shift of charges in the presence of visible light. The average reduction of chemical oxygen demand (COD) was found to be 75% after irradiation with direct sunlight. In the degradation process of dyes, superoxide anion radicals were the main responsive species, as revealed by trapping experiments. The degradation efficiency of MnV$_2$O$_6$/BiVO$_4$ heterojunction did not diminish even after four cycles. In addition, the catalytic performance of the fabricated heterojunction was also explored for reducing 4-nitrophenols (4-NP) by using NaBH$_4$. Absolute conversion of 4-NP to 4-aminophenol (4-AP) occurred without the production of intermediate byproducts.

1. Introduction

A clean environment is highly significant for healthy living and sustaining life on earth. As a whole, all living creatures are reliant on the environment for food, air, water, and many other requirements. Consequently, it is significant that each individual must contribute to save and protect the environment from various pollutants. Very important assets for life like water and air are under continuous threat from various organic pollutants and toxic chemicals generated from the chemical, agricultural, food and textile industries that act as poisons.[1,2] Carcinogenic dyes present in water restrict the path of sunrays and obstruct them from entering the aqueous system. This results in a reduced rate of photosynthesis and damage to aquatic animals.[3] In addition to the impairment of body organs, dyes also affect public health by accumulation in living beings. Nitrophenol compounds are widely used in the synthesis of

agrochemicals, fungicides and rubber. These are considered to be persistent pollutants and adversely affect the functioning of various body organs. An eco-friendly approach must be planned to carry out degradation reactions more precisely and efficiently for elimination of these toxic chemicals from waste water. Previously used conventional methods such as biological degradation, membrane filtration, chemical oxidation, and plasma ozonization have not been proved to be appropriate due to their complexity, low efficiency, time consuming mechanisms, disposal problems and being uneconomical.[4,5]

Among all the natural energy resources, solar energy is considered to be the most efficient, easily available and renewable energy source on earth. In the whole solar spectrum, 43% energy is provided by visible light whereas UV region contributes only 4% of energy.[6,7] In this manner, improvement of effective photocatalysts, especially noticeable light responsive systems, is fundamental for the proficient usage of sunlight-based energy in photocatalysis. The general mechanism of photocatalysis involves the generation of activated electron–hole pairs in the valence band of semiconductor, followed by electron transfer from the valence band to the conduction band in the presence of light energy.[8] These charged species play a major role in photocatalysis by providing surface

[a]Department of Chemistry, Sri Guru Granth Sahib World University, Fatehgarh Sahib, Punjab, India. E-mail: dhillonps2003@gmail.com; kaushalsandeep33@gmail.com

[b]School of Chemistry & Biochemistry, Thapar Institute of Engineering and Technology, Patiala, India

† Electronic supplementary information (ESI) available. See DOI: 10.1039/d1na00499a

for adsorption of species, and generate superoxide and hydroxide radicals which further participate in oxidation–reduction degradation reactions.

In past years, removal of pollutants by the photocatalytic process has become a matter of great interest. Until now, a number of semiconductor photocatalysts have been fabricated to remove toxic chemicals from the environment. TiO_2, ZnO, CuO, SnO_2, ZnS, CdS, $BiVO_4$, and $g-C_3N_4$ are considered to be the most common semiconductors utilized for light energy mediated catalytic reactions.[9–12] Out of all the semiconductor photocatalyst materials, $BiVO_4$ has gained maximum attraction because of its excellent photocatalytic activity in visible light region, low toxicity and high stability.[13] $BiVO_4$ has a band gap of 2.44 eV that corresponds to λ_{max} value between 300 and 400 nm. Its photocatalytic behavior promotes removal of toxic dyes, pesticides, disintegration of pollutants and production of hydrogen gas by splitting of water. One major limitation concerning its efficiency was a high rate of recombination of electron–hole pairs which retards its capability. This limitation was overcome by modifying the structure of $BiVO_4$ by doping with metals and non-metals or coupling with other semiconductors. With these efforts, the structure and morphology of $BiVO_4$ were tuned for its utilization as a photocatalyst in the presence of visible light. To date, a number of $BiVO_4$ based hybrid composites have been manufactured which exhibited higher photocatalytic activity towards photo-electrochemical reactions, dye degradation, mineralization of pesticides and, splitting of water as compared to that of pure $BiVO_4$ semiconductor.[14–21]

In the present investigation, a sunlight activated heterojunction, $MnV_2O_6/BiVO_4$, was synthesized by a one pot hydrothermal method. The p-type MnV_2O_6 photocatalyst comprises narrow band gap energy ($\sim$1.6 eV) and exhibits high catalytic activity towards redox reactions involving splitting of water into hydrogen and oxygen, elimination of harmful pesticides, and degradation of toxic organic dyes under visible radiation.[22–24] In addition to this, MnV_2O_6 also acts as an excellent anodic material in lithium-ion batteries, attributed to its continuous recycling activity.[25] The prepared $MnV_2O_6/BiVO_4$ heterojunction was utilized as a photocatalyst for degrading MB and RhB dyes, and reducing 4-NP in the presence of solar radiation. Photocatalytic experiments under same conditions were performed for sole $BiVO_4$ and MnV_2O_6 also.

2. Experimental

2.1 Materials and methods

$Bi(NO_3)_3 \cdot 5H_2O$, NH_4VO_3, $Mn(CH_3COO)_2 \cdot 4H_2O$, $NaBH_4$, polyvinylpyrrolidone (PVP), 4-nitrophenol, and MB and RhB dyes were purchased from LOBA Chemie Pvt Ltd India.

2.1.1 Synthesis of $BiVO_4$. Synthesis of pure $BiVO_4$ was carried out by adding 0.2425 g of $Bi(NO_3)_3 \cdot 5H_2O$ in 30 mL of distilled water while maintaining the temperature at 50 °C. In another beaker, 10 mL solution was made by adding 0.0585 g of NH_4VO_3. Then, slow mixing of the above solutions was carried out with continuous magnetic stirring for 30 min (pH = 2), followed by addition of PVP surfactant. The obtained mixture was transferred to a steel autoclave that was heated in an oven

maintained at 180 °C. The obtained yellow-colored precipitates were thoroughly rinsed with distilled water and dried in an oven at 100 °C for 2 h (sample S-I).
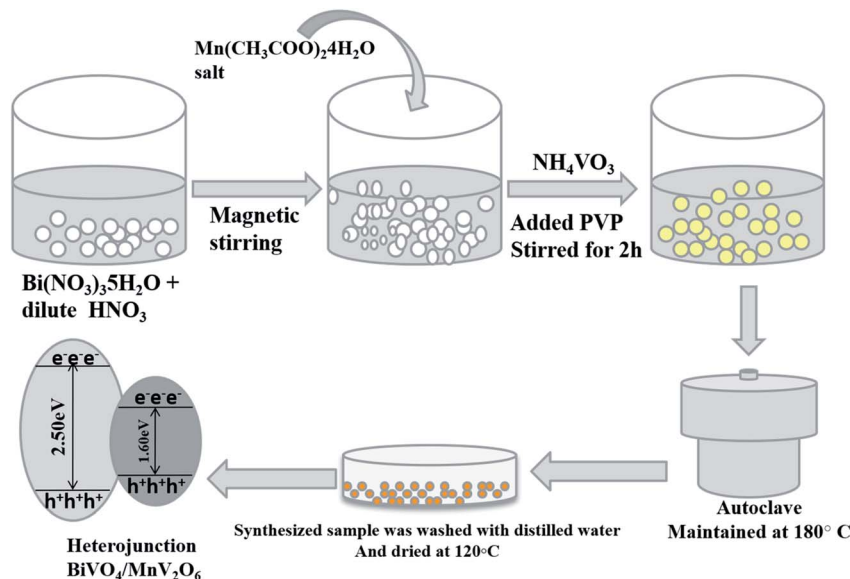
2.1.2 Synthesis of MnV_2O_6. In this hydrothermal synthesis, a solution of 0.306 g of $Mn(CH_3COO)_2 \cdot 4H_2O$ in 50 mL distilled water was prepared and stirred for 30 min. To this solution, 0.29 g of NH_4VO_3 was added and stirring was continued. Then, PVP was added to prevent agglomeration of particles. The obtained blend was transferred to an autoclave and heated at 80–180 °C in an oven. The precipitates (brown colored) obtained were washed with distilled water and dried at 50 °C for 5 h (sample S-II).

2.1.3 Fabrication of $MnV_2O_6/BiVO_4$ heterojunction. A one pot hydrothermal method was utilized to prepare the $MnV_2O_6/BiVO_4$ heterojunction with different molar ratios. A solution of $Bi(NO_3)_3 \cdot 5H_2O$ in dilute HNO_3 was prepared and magnetically stirred till a clear suspension was obtained. Then, $Mn(CH_3COO)_2$ was added and mixed thoroughly with magnetic stirring. An aqueous solution of NH_4VO_3 (50 mL) was prepared separately and added drop wise to the above mixture with continuous stirring. PVP was also added in the mixture to synthesize the composite with an optimum particle size and structure. After 2 h of continuous stirring, this mixture was transferred to an autoclave and placed overnight in an oven at 180 °C. The obtained precipitates were washed thoroughly with double distilled water (DDW) and dried in an oven for 5 h at 100–120 °C. By following the same procedure, composites with different molar ratios of $MnV_2O_6 : BiVO_4$ $i.e.$, 0.25 : 1.00, 0.50 : 1.00, 0.75 : 1.00, and 1.00 : 1.00 were synthesized by varying the amounts of reagents and labeled as S-III, S-IV, S-V and S-VI, respectively (Scheme 1).

2.1.4 Characterization of $MnV_2O_6/BiVO_4$ heterojunction. A Bruker Alpha-T spectrometer was employed to obtain FT-IR spectra of the synthesized heterojunction samples. UV-visible spectra of the fabricated heterojunction and organic dyes were obtained on a Shimadzu/UV-2600 UV-vis spectrophotometer at high resolution in a scan range of 200–800 nm using a transparent quartz cuvette of 1 cm width. An X-ray diffractometer was used to obtain XRD powder patterns of pure as well as doped samples. Topographic details of the heterojunction samples were visualized by using a FESEM, Carl Zeiss Supra 55 equipped with an EDS to perform elemental and chemical analysis of the samples. Highly magnified TEM images of the internal structure and size of particles were obtained using a JEOL JEM 2100 PLUS. The photoluminescence (PL) spectra were obtained at room temperature using a spectrofluorometer (HORIBA Fluoromax plus CP-011).

2.1.5 Photocatalysis experiments. The photocatalytic performance of the synthesized $BiVO_4$, MnV_2O_6 and $MnV_2O_6/BiVO_4$ heterojunction samples with different molar ratios was estimated by degradation of organic dyes MB and RhB in natural sunlight. Day light from 9:30 am to 2:30 pm was utilized to perform the photocatalytic experiments. In this typical reaction, 50 mL solution of the organic dye MB (25 mg L^{-1}) was prepared in DDW with continuous magnetic stirring for 20 min. To this solution, 50 mg of the synthesized catalyst was added. Then, the solution was placed in natural sunlight. At standard

Scheme 1 Schematic representation of the synthesis of MnV_2O_6/$BiVO_4$ heterojunction using a hydrothermal method.

time spans, 5 mL of this solution was taken out, filtered to eliminate the catalyst and then centrifuged for 10 min. The progress of degradation was monitored by determining the absorbance of this centrifuged solution. The photocatalytic efficiency of pure $BiVO_4$ and pure MnV_2O_6 was compared by degrading MB and RhB dyes separately, under identical reaction conditions.

2.1.6 Photocatalytic reduction test of 4-nitrophenol. The catalytic performance of MnV_2O_6/$BiVO_4$ heterojunction for reduction was investigated using 4-nitrophenol (4-NP). In this process, a freshly prepared solution of $NaBH_4$ (1.0 mM) in distilled water was thoroughly mixed with a 50 mL solution of 4-NP (0.2 mM) in a beaker, and stirred on a magnetic stirrer. The colour of the solution instantly transformed to colorless from yellow. Subsequently, 15 mg of the heterojunction was put into the above solution. The reaction progress at room temperature was monitored by using a UV-visible spectrophotometer after equal gaps of time.

3. Results and discussion

The as-synthesized MnV_2O_6/$BiVO_4$ heterojunction was characterized using various sophisticated techniques like UV, FTIR, XRD, FESEM, HRTEM and XPS. UV-vis diffuse reflectance spectroscopy (DRS) of S-I to S-VI samples was performed and the results are displayed in Fig. S1 (ESI†). The band gap (E_g) values of $BiVO_4$ and MnV_2O_6 were found to be 2.5 eV & 1.60 eV, respectively, which agree with previous findings.[22,26] The band gap of MnV_2O_6/$BiVO_4$ heterojunction samples *i.e.* S-III to S-VI was found to be 2.2, 2.1, 1.95 and 1.90 eV, respectively, signifying that the incorporation of MnV_2O_6 diminishes the band gap of $BiVO_4$. Moreover, this diminution affirms electronic coupling between MnV_2O_6 and $BiVO_4$.

FTIR spectra of pure $BiVO_4$, MnV_2O_6 and MnV_2O_6/$BiVO_4$ heterojunctions with varied molar ratios are shown in Fig. 1.

The band in the 600–800 cm^{-1} region was assigned to symmetric and asymmetric vibrations of the VO_4^{3-} group. The peak at 750 cm^{-1} is attributed to the vibrations of Bi–V bonds, and stretching vibration of the V–O double bond is present at 1366 cm^{-1}.[27] The sharp peaks in 600–1000 cm^{-1} region for MnV_2O_6 are attributed to the vibrations of V–O–V bonds. Short V–O bonds gave an absorption band at 903 cm^{-1} and that of longer V–O bonds appeared at 815 cm^{-1}. In the FTIR spectra of MnV_2O_6/$BiVO_4$ heterojunction samples with different molar ratios, some additional peaks were observed as the amount of MnV_2O_6 increased. This observation confirmed that no structural change happened in the synthesized heterojunction composite. Sharp peaks in the region 1500–1550 cm^{-1} were
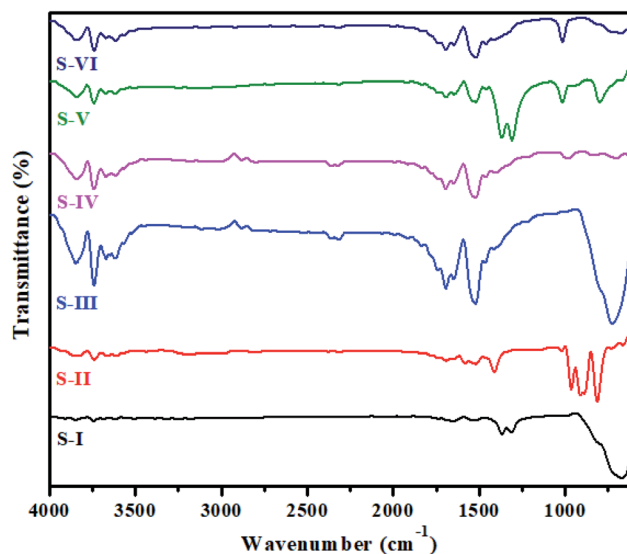

Fig. 1 FTIR spectra of pure $BiVO_4$ (S-I), MnV_2O_6 (S-II) and MnV_2O_6/$BiVO_4$ heterojunction samples (S-III to S-VI).

observed for all composites and correspond to interactions of two metals. A clear sharp band at 1700 cm^{-1} could be attributed to the metal–oxygen stretching vibrations. The O–H stretching vibrations of lattice water molecules were observed at 3750 cm^{-1}. Change in the peak intensity of $BiVO_4$ was noticed which might be due to the interactions of both the semiconductors through the formed interface. IR data of composites with different molar ratios confirmed that both $BiVO_4$ and MnV_2O_6 semiconductors coexist in the composite.

The XRD patterns of synthesized $BiVO_4$, MnV_2O_6 and $MnV_2O_6/BiVO_4$ heterojunctions are shown in Fig. 2. It can be noticed from the XRD pattern of $BiVO_4$ semiconductor (Fig. 2S-I) that the diffraction peaks can be entirely indexed to a monoclinic phase (JCPDS card-96-901-3438). The corresponding peaks are displayed in the XRD spectrum of $BiVO_4$ at $2\theta = 18.7$ (4.74 Å), 28.9 (3.07 Å), 30.7 (2.92 Å), 34.6 (2.59 Å), 35.3 (2.54 Å), 39.7 (2.26 Å), 42.3 (2.13 Å), 46.7 (1.94 Å), 50.3 (1.81 Å), 53.5 (1.71 Å), 58.7 (1.54 Å) and 59.6 (2.1 Å) with indices (110), (−221), (040), (200), (−202), (−311), (150), (240), (−402), (310), (−421) and (042), respectively. The XRD pattern of MnV_2O_6 semiconductor (Fig. 2S-II) clearly shows that the diffraction peaks match the provided data remarkably well (JCPDS card-96-711-9177), and no phase impurity was observed. The corresponding peaks are exhibited in the XRD spectra of MnV_2O_6 at $2\theta = 9.5$ (9.25 Å), 11.5 (7.65 Å), 17.5 (5.07 Å), 19.2 (3.45 Å), 25.8 (3.34 Å), 27.1 (3.29 Å), 28.3 (3.16 Å), 28.9 (2.13 Å), 31.5 (2.83 Å), 33.4 (2.67 Å), 35.0 (2.56 Å), 52.1 (1.75 Å) and 53.4 (1.71 Å) with indices (001), (100), (101), (002), (102), (011), (201), (003), (−112), (−302), (103), (401) and (−121), respectively. When a small amount of MnV_2O_6 was introduced, no diffraction peaks of MnV_2O_6 were observed in the XRD pattern of $MnV_2O_6/BiVO_4$ heterojunction (Fig. 2S-II). With an increase of MnV_2O_6 content, S-III, S-IV, S-V and S-VI

displayed diffraction peaks of both $BiVO_4$ and MnV_2O_6, demonstrating the effective fabrication of $MnV_2O_6/BiVO_4$ heterojunction. In order to find typical crystallite size of the samples, Debye–Scherer equation was employed.[28,29] The crystallite sizes were observed as 32.7 (S-I), 34.01 (S-II), 31.35 (S-III), 25.49 (S-IV), 40.6 (S-V) and 40.1 nm (S-VI).

FESEM was performed to explore the morphology of synthesized heterojunction (Fig. 3a and b). The $MnV_2O_6/BiVO_4$ heterojunction demonstrated a belt-like morphology with a length of 8–10 μm (Fig. 3a). Fig. 3b illustrates that the $MnV_2O_6/BiVO_4$ nano-belts were homogeneously mixed to form an interface between the two materials *i.e.*, MnV_2O_6 and $BiVO_4$, and the thickness of nanobelts was tens of nanometers. The FESEM micrograph of pure $BiVO_4$ nanoparticles displayed a rod like structure with a high degree of homogeneity. Pure MnV_2O_6 nanoparticles have a globular structure with agglomeration (Fig. S2†). The morphology of the heterojunction was further explored by HRTEM (Fig. 3c and d). It was revealed that MnV_2O_6 particles were homogeneously mixed with $BiVO_4$ nanoparticles, and particle size of the resulting composite material was in 35–45 nm range which is comparable to that obtained from the XRD results. The corresponding SAED pattern showed clear ring patterns confirming the formation of polycrystalline $MnV_2O_6/BiVO_4$ heterojunction.

The chemical states of as-synthesized $MnV_2O_6/BiVO_4$ heterojunction were examined by XPS. Elements C, Mn, V, O and Bi were confirmed by the survey scan of XPS spectra (Fig. 4a). The high-resolution C 1s spectrum of $MnV_2O_6/BiVO_4$ heterojunction (Fig. 4b) may be deconvoluted into two dissimilar peaks at 286.8 eV and 284.5 eV which are attributed to epoxide C (O–C–O) and C=C sp^2 hybridized material, respectively.[30] Peaks at 529.5 and 530.78 eV in the O 1s spectrum (Fig. 4c) are ascribed to the
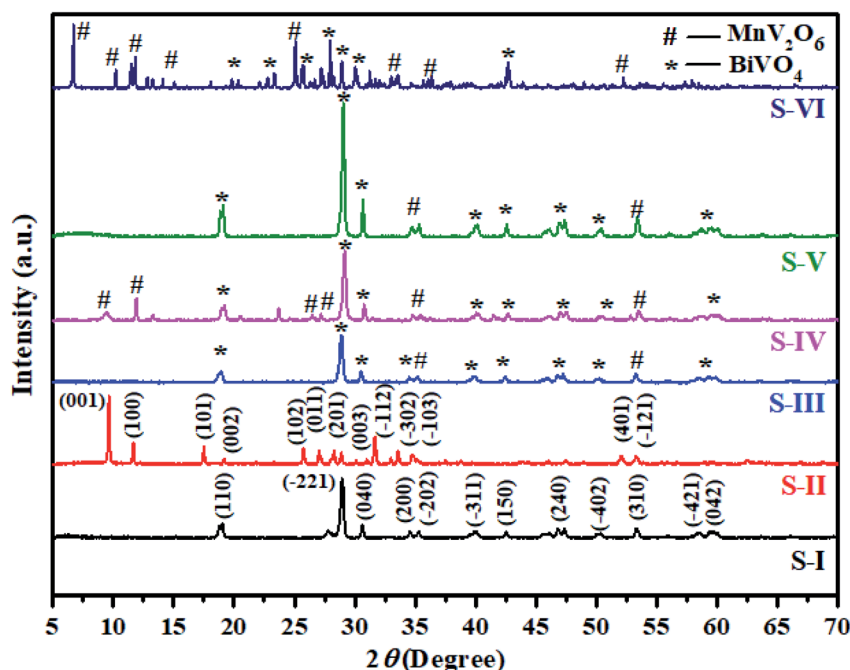

Fig. 2 XRD patterns of pure $BiVO_4$ (S-I), MnV_2O_6 (S-II) and $MnV_2O_6/BiVO_4$ heterojunction samples (S-III to S-VI).
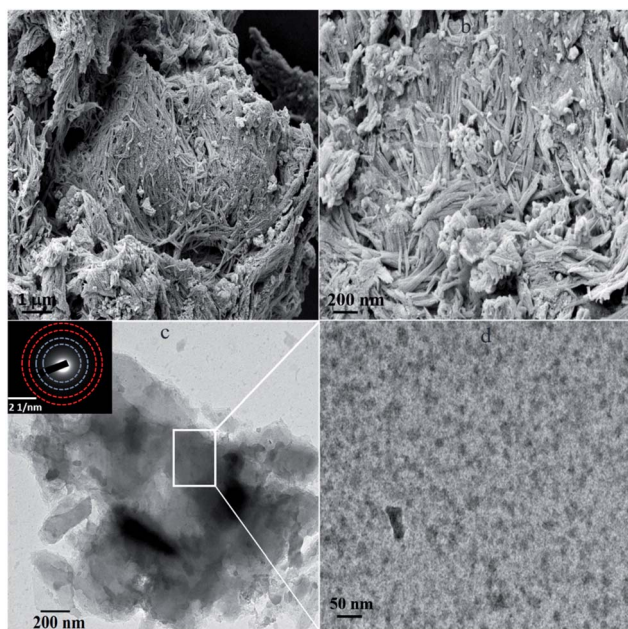
Fig. 3 (a and b) FESEM images and (c and d) HRTEM images (inset SAED pattern) of $MnV_2O_6/BiVO_4$ heterojunction.

oxygen bonded inside an oxide crystal (O^{2-}) in the composite, and –OH groups adsorbed on the surface, respectively.[31,32] For the V 2p orbital (Fig. 4d), binding energy peaks at 524.1 eV and 516.7 eV relate to V, $2p_{1/2}$ and V, $2p_{3/2}$ which originate from V^{5+}.[33] Mn 2p XPS spectrum (Fig. 4e) displayed two obvious peaks at 645.4 and 653.4 eV, related to Mn, $2p_{3/2}$ and Mn, $2p_{1/2}$, respectively, arising from Mn^{2+}.[25] In case of Bi (Fig. 4f), peak at 158.7 eV was attributed to the binding energy of Bi $4f_{7/2}$ whereas the peak at 164.04 eV was ascribed to Bi $4f_{5/2}$. The chemical states of as-synthesized MnV_2O_6 and $BiVO_4$ nanoparticles were also examined by XPS. Elements C, Mn, V and O and C, V, Bi and O were confirmed by the survey scan of XPS spectra in MnV_2O_6 and $BiVO_4$ nanomaterials, respectively (Fig. S3†).

The porosity of $MnV_2O_6/BiVO_4$ heterojunction was established by the N_2 adsorption–desorption experiment. According to the IUPAC classification, this sort of isotherm is extremely close to the type II adsorption isotherm (Fig. 5). The specific surface area, total pore volume and micropore volume noticed from BET were 77.35 m^2 g^{-1}, 0.2331 cm^3 g^{-1} and 0.00075 cm^3 g^{-1}, respectively. The mean pore diameter was determined to be 5.61 nm. Hence, $MnV_2O_6/BiVO_4$ heterojunction has a high precision external zone and adequate pore structure which is extremely useful in surface interaction activities.

Photochemical properties of semiconductors and their corresponding hybrid materials were studied with photo-luminescence (PL) spectroscopy. The electrons and holes on excitation, started moving from the ground energy level to a higher energy level and recombined again.[34,35] During return to the ground state, various emissions are generated, depending upon band gap energy values of the semiconductor. The intensity of these emissions can be recorded corresponding to their wavelength values using the PL technique, and based on

their intensity, the rate of recombination of active charged species can be detected. The PL spectra of pure $BiVO_4$, pure MnV_2O_6, and $BiVO_4/MnV_2O_6$ heterojunction are shown in Fig. S4.† For the pure $BiVO_4$ semiconductor material, excitation occurred at 325 nm wavelength and corresponding to this excited energy, a broad band in the region of 550–650 nm was produced in the emission spectrum. Pure MnV_2O_6 showed excitation at 450 nm and delivered a highly intense peak at 562 nm. The intensity of these pure compounds was much higher as compared to that of the hybrid $BiVO_4/MnV_2O_6$ heterojunction photocatalyst which confirmed successful separation of active charged species (electron–hole pairs) and reduced recombination rate which favored high photocatalytic activity of the heterojunction.

3.1 Photocatalytic reduction of 4-nitrophenol over $MnV_2O_6/BiVO_4$ heterojunction

The waste water disposed off by industries probably contains hazardous nitrophenols and their derivatives. The main sources of nitrophenols and their derivatives are insecticide, synthetic dye and herbicide manufacturing industries.[36] Hence, the elimination of these hazardous chemicals from industrial effluents is vital before it is discharged into water bodies.

However, it is hard to remove these compounds by regular microbial degradation due to their natural and artificial stability.[37] Thus, it is essential to build up environment responsive strategies to remove such contaminants from waste effluents.[38] UV-visible spectra during the reduction of 4-nitro-phenol (4-NP) by $NaBH_4$ using $MnV_2O_6/BiVO_4$ heterojunction as a catalyst are given in Fig. 6. The absorption peak of the aqueous solution of yellow coloured 4-NP was observed at 317 nm. When an aqueous solution of $NaBH_4$ was added, a red-shift was noticed at ~400 nm owing to the generation of nitrophenolate anion (Fig. S5†). The absorption peak at 400 nm remained invariable for a prolonged period, suggesting that 4-nitro-phenolate ions could not be reduced by sole $NaBH_4$ in the absence of as-synthesized catalyst. Pure MnV_2O_6 and $BiVO_4$ nanoparticles illustrated little activity and hence, both of them can't be considered worthwhile catalysts for 4-NP reduction. However, 4-NP was effortlessly reduced using both, $NaBH_4$ and $MnV_2O_6/BiVO_4$ heterojunction. The absorption peak corresponding to 4-NP at 400 nm progressively diminished and almost vanished after 40 min (Fig. 6a). Meanwhile, another absorption peak at ~297 nm corresponding to 4-aminophenol (4-AP) with increasing intensity emerged. This outcome confirmed the comprehensive transformation of 4-NP to 4-AP without the production of intermediates as established in earlier reports also.[39] Absorbance and concentration of the solution are proportionate to each other and hence, absorbance A_0 ($t = 0$) corresponds to the initial concentration, and absorbance A_t corresponds to the concentration at time t (C_t). The rate constant (k) was evaluated from the plot of $\ln(C_t/C_0)$ vs. time (min) and its values were determined to be 0.0118, 0.0120, 0.008, 0.030, 0.12 and 0.045 min^{-1} for S-I, II, III, IV, V and VI, respectively for reduction of 4-NP (Fig. 6b).
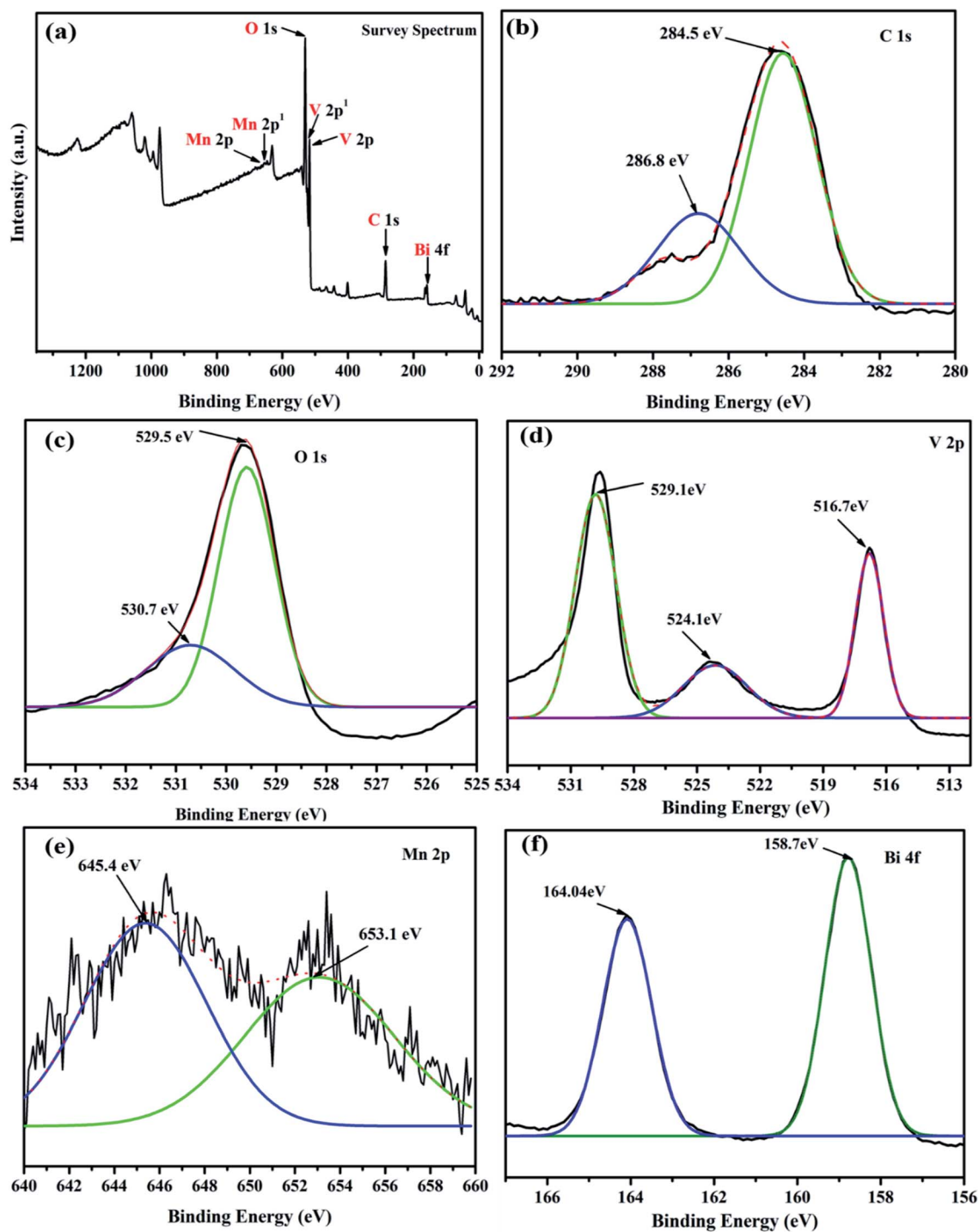
Fig. 4   XPS spectra of $MnV_2O_6/BiVO_4$ heterojunction (S-V).

3.2   Photocatalysis of dyes over $MnV_2O_6/BiVO_4$ heterojunction

The photocatalytic activities of pure MnV_2O_6 and $BiVO_4$ semiconductors as well as those of $MnV_2O_6/BiVO_4$ heterojunctions were assessed by degrading MB and RhB dyes in solar light. The photocatalytic performance of $MnV_2O_6/BiVO_4$ heterojunctions was optimized w.r.t. solution pH, varying photocatalyst dosage and lapse of time, to achieve maximum degradation.

The degradation results were recorded over a wide range of photocatalyst amounts and pH. It was noticed that dye degradation performance varied as a function of the amount of $MnV_2O_6/BiVO_4$ heterojunction photocatalyst. As expected, the amount of $MnV_2O_6/BiVO_4$ heterojunction photocatalyst for the degradation of both MB and RhB dyes followed the order: 50 > 40 > 30 and 20 mg. The increase in photocatalyst amount from 20 mg to 50 mg leads to an increase in dye degradation from 25
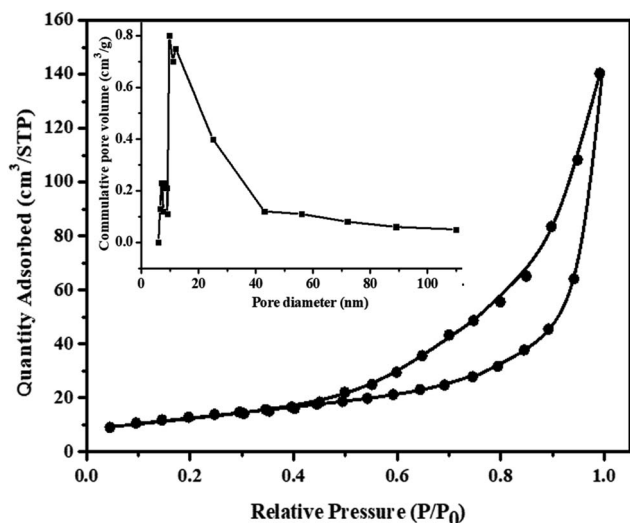
Fig. 5 N_2 adsorption–desorption isotherm curves of $MnV_2O_6/BiVO_4$ heterojunction (S-V); inset: pore size distributions.

to 98.1% and 23 to 96.2%, respectively, for MB and RhB dyes. Evidently, the enhancement of degradation proficiency with an increase in the amount of heterojunction is primarily attributed to the increased number of active sites on the surface of $MnV_2O_6/BiVO_4$ photocatalyst for UV light absorption.

The pH of solution is another most essential factor in photocatalytic degradation. Fig. S6† presents the effect of pH (range 3–10) on the degradation of both the dyes over $MnV_2O_6/BiVO_4$ heterojunction photocatalyst. It was observed that both the MB and RhB dyes degraded to a maximum extent at pH 7 compared to lower or higher pH values. This behavior might be due to the formation of Fenton's reagent at a lower pH and at a higher pH, $MnV_2O_6/BiVO_4$ photocatalyst could leach into solution and form chemical sludge.[40] Therefore, it was found that the as-synthesized photocatalyst was more efficient at pH 7.

The photocatalytic degradation of aqueous solutions of MB and RhB dyes over $MnV_2O_6/BiVO_4$ heterojunction photocatalyst as a function of time was examined by UV-visible spectroscopy (Fig. S7†). A drastic decrease in absorption peak intensity with time was noticed, and the peak nearly disappeared within 6 and 35 min, respectively, for MB and RhB dyes.

It is clear from Fig. 7a that pure semiconductors $BiVO_4$ (S-I) and MnV_2O_6 (S-II), and heterojunction photocatalysts, S-III, IV, V & VI have degraded 56, 45, 70, 86, 98 & 98.5% of MB dye after 6 min of sunlight irradiation. To endorse the self-photosensitization methodology, a blank experiment was likewise accomplished in the absence of catalyst under identical experimental conditions, and negligible degradation was noticed. When the catalyst was added to the dye solution, significant dye degradation was observed, indicating that the photocatalytic measure is largely responsible for dye degradation. To further investigate the photocatalytic efficiency of $MnV_2O_6/BiVO_4$ heterojunction composite, the COD experiment was performed. The calculated COD value for MB and RhB solutions decreased from 160 to 40 mg L^{-1} and 115 to 37 mg L^{-1}, respectively. These results showed that the mineralization yield of composite reached a value of 75% and 68%, respectively, for MB and RhB dyes, after irradiation with direct sunlight.

In addition, kinetic models were employed to comprehend the photocatalytic degradation process of MB dye. Similarly, a comparable performance for degradation of RhB dye under solar light in the presence of $MnV_2O_6/BiVO_4$ heterojunction photocatalyst was observed (Fig. 7b). It was demonstrated from Fig. 7b that the intensity of absorption peak diminished appreciably with the passage of time, signifying the efficient disintegration of RhB dye using the $MnV_2O_6/BiVO_4$ heterojunction photocatalyst. The debasement productivity of RhB dye over S-I, II, III, IV, V & VI was determined to be 47, 45, 58.7, 96 and 96.1%, respectively, after 35 min of sunlight irradiation.
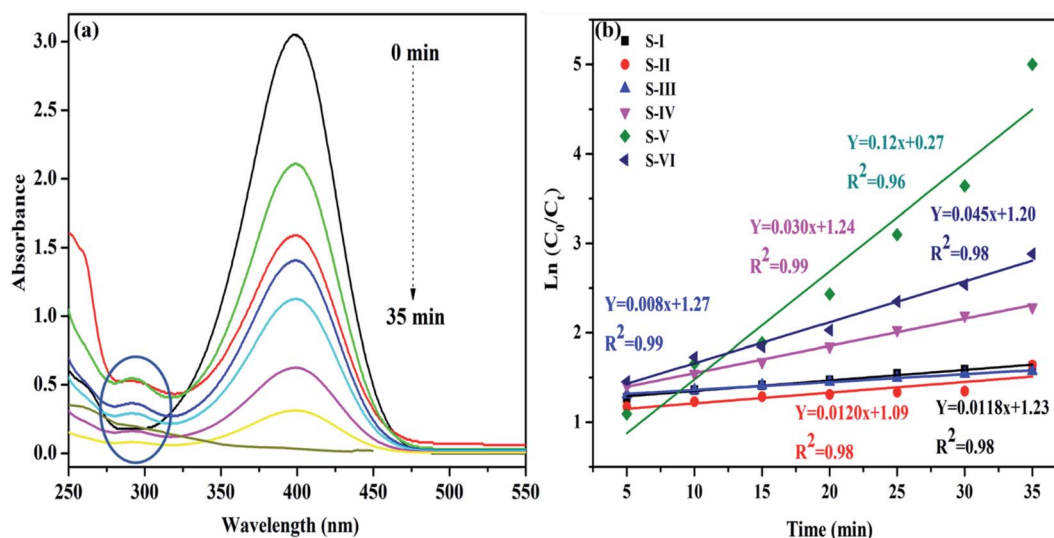

Fig. 6 (a) Reduction of 4-nitrophenol with $NaBH_4$ over $MnV_2O_6/BiVO_4$ heterojunction shown by changes in UV-vis spectra; (b) graph of $\ln(C_0/C_t)$ vs. time.
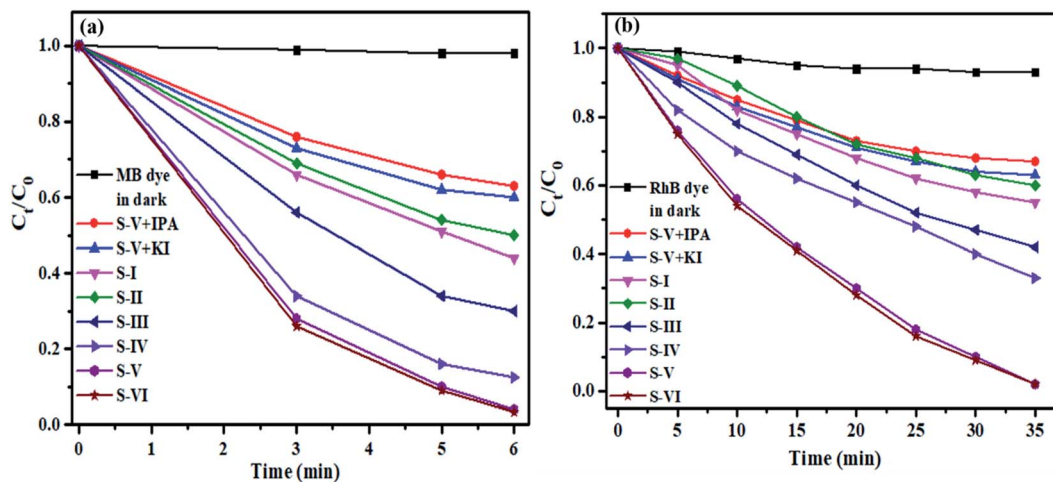
Fig. 7 Plot illustrating the concentration change of the MB and RhB dyes as a function of time of irradiation.

In the heterogenous photocatalytic degradation process of organic pollutants, various active species comprising superoxide ($\cdot O_2^-$) anion radicals, hydroxide ($\cdot OH$) radicals, and photo-generated electrons (e^-) and holes (h^+) are created under appropriate light irradiation.[41] To figure out the active species that assumes a significant role in dye photodegradation utilizing $MnV_2O_6/BiVO_4$ heterojunction on irradiation by sunlight, different types of examinations on extinguishing active species were carried out by addition of separate scavengers in the reaction mixture. For this purpose, isopropyl alcohol (IPA), potassium iodide (KI) and benzoquinone (BQ) were employed for scavenging $\cdot OH$, h^+ and $\cdot O_2^-$ radicals, respectively. Due to extinguishing of active species, photocatalytic response is little restrained and prompts modest degradation of both the dyes. The degree of decline brought about by scavengers in degradation demonstrated the role of competing responsive species.

Fig. 7(a) and (b) illustrate that photodegradation of both the dyes over $MnV_2O_6/BiVO_4$ heterojunction was considerably influenced on addition of scavengers. The degradation of dyes was significantly suppressed on addition of BQ ($\cdot O_2^-$ scavenger) which indicated a crucial role of $\cdot O_2^-$ in the photodegradation procedure. The photodegradation activity of $MnV_2O_6/BiVO_4$ only marginally decreased on introducing IPA and KI which suggested that both $\cdot OH$ and h^+ have a minor but synergistic role in the degradation reaction.[36,42]

3.3 Plausible mechanism of photodegradation

In the light of results obtained, a tentative mechanism has been suggested to clarify the improved photocatalytic activity of $MnV_2O_6/BiVO_4$ heterojunctions (Fig. 8). To perceive the band positions of $MnV_2O_6/BiVO_4$ heterojunctions, the potentials at conduction band (CB) and valence band (VB) edges of MnV_2O_6 & $BiVO_4$ semiconductors were designed using the equations below:[23]

$$E_{CB} = \chi - E^e - 0.5E_g \tag{1}$$

$$E_{VB} = E_{CB} + E_g \tag{2}$$

where E_{CB}, E_{VB}, E^e and χ denote the potential of CB & VB bands, energy of free electrons vs. hydrogen (4.5 eV) and electronegativity (χ) of the semiconductor, respectively.[43] The following equation was used to get the value of χ:

$$\chi = [\chi(A)^a \chi(B)^b]^{1/[a+b]} \tag{3}$$

The constants a and b denote the number of atoms in the compounds.[44] E_g, χ, E_{CB} and E_{VB} values for $BiVO_4$ were found to be 2.50 eV, 6.04 eV, +0.29 and +2.79 eV/NHE, respectively and are comparable to the reported values.[45,46] The values of E_g and χ for MnV_2O_6 are 1.60 eV and 5.90 eV, respectively. Consequently, E_{CB} and E_{VB} values for MnV_2O_6 were determined to be +0.60 and +2.20 eV/NHE.

In the light of above discussion and knowledge of active species involved, a potential mechanism for the degradation of organic dyes utilizing $BiVO_4/MnV_2O_6$ heterojunction has been projected as follows and is displayed in Fig. 8. When sunlight was
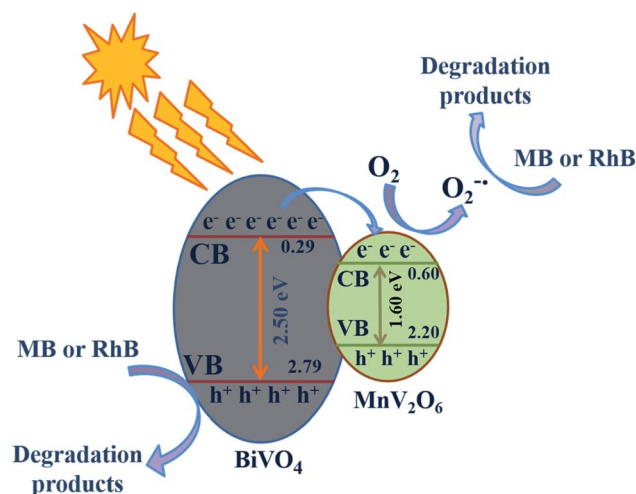

Fig. 8 A plausible mechanism for organic pollutant removal over $BiVO_4/MnV_2O_6$ heterojunction under direct sunlight illumination.

Table 1 Comparison of heterojunctions for photocatalytic degradation of organic contaminants

Sr. no.	Photocatalyst	Method of synthesis	Catalyst dosage (mg)	Pollutant/conc.	Source of light/time in min	Photocatalytic efficiency (%)	Ref.
1	ZnO/Ag_2O	Photochemical route	20	MB/3.12×10^{-5} mol L^{-1}	250 W UV, 500 W Xe lamp/4	99.5	47
2	$AgBr/Bi_2WO_6$	Hydrothermal	200	MB/10 mg L^{-1}	500 W Xe lamp/30 min	100	48
3	Ag_2O/TiO_2	Sol gel	10	4-NP/200 ppm	Solar/210 s	100	49
4	$Ni_2P/Ni_{12}P_5$	Solvothermal	1.5	4-NP/14 mg L^{-1}	Solar/8 min	100	50
5	CuO/ZnO	Hydrothermal	30	MB/5 mg L^{-1}	Solar radiation/210 min	97	51
6	$CuSbSe_2/TiO_2$	Microwave method	100	RhB/MB/100 ppm	Long UV-A radiation/275 min	75.93 (RhB), 42.72 (MB)	52
7	$CuO/g\text{-}C_3N_4$	Ultrasonic	10	4-NP/20 ppm	35 W Xe lamp/100 min	92	53
8	$Ag\text{--}CuO/g\text{-}C_3N_4$	Hydrothermal	100	4-NP/100 ppm	Ni light irradiation/4 min	97.8	54
9	$CeO_2/CuO/Ag_2CrO_4$	Chemical precipitation	125	MB (5 mg L^{-1})/RhB (10 mg L^{-1})	LED lamp/80 min	58.46 (MB), 84.79 (RhB)	55
10	$Bi_2Zr_2O_7/CdCuS$	Hydrothermal	50	RhB/MB & 4-NP	Solar light/200 min	84 (RhB), 90 (MB), 100 (4-NP)	56
11	$WO_3\text{-}BPNs$	Co-precipitation	50	RhB/10 mg L^{-1}	350 W Xe lamp/120 min	92	57
12	$MOF/P\text{--}TiO_2$	Self-assembly hydrothermal	10	RhB/10 ppm	300 W Xe/25 min	97.6	58
13	$MnV_2O_6/BiVO_4$	One pot hydrothermal	50	4-NP, MB & RhB (25 mg L^{-1})	Direct sunlight, 35 (4-NP), 6 (MB), 35 RhB	100 (4-NP), 98 (MB), 96 (RhB)	Present work
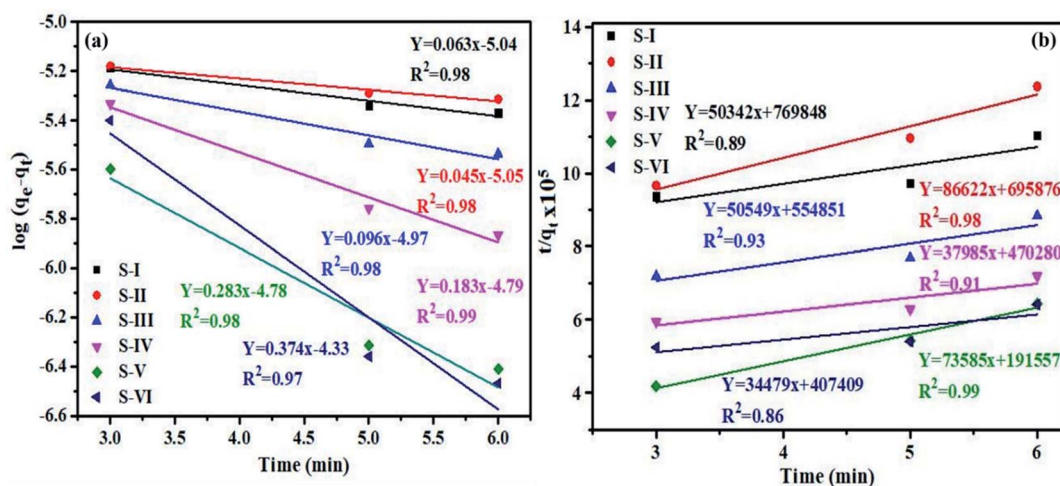
Fig. 9 Graph of (a) pseudo first and (b) second order kinetics models for degradation of MB dye over $MnV_2O_6/BiVO_4$ heterojunction.

illuminated over $BiVO_4/MnV_2O_6$ heterojunction, the photons approaching the photocatalyst were hopefully consumed by $BiVO_4$ and MnV_2O_6 counterparts, prompting the production of a few electron–hole pairs. $BiVO_4$ has a high negative flat band capability in comparison to MnV_2O_6. As a result, the electrons continue to move towards MnV_2O_6 from $BiVO_4$ till the Fermi level stability of both is accomplished. Concurrently, $OH^{\cdot}$ is generated by oxidation of adsorbed H_2O molecules by the photoinduced holes of the VB of MnV_2O_6 and $BiVO_4$ semiconductors. Simultaneously, the electrons gathered on the exterior of MnV_2O_6 interact with the adsorbed oxygen to generate $^{\cdot}O_2^{-}$. Hence, the produced active species like $OH^{\cdot}$, h^+ and $^{\cdot}O_2^{-}$ efficiently break down the dye molecules to CO_2, H_2O and non-toxic inorganic

Table 2 Various factors of the kinetic models for degradation of MB dye

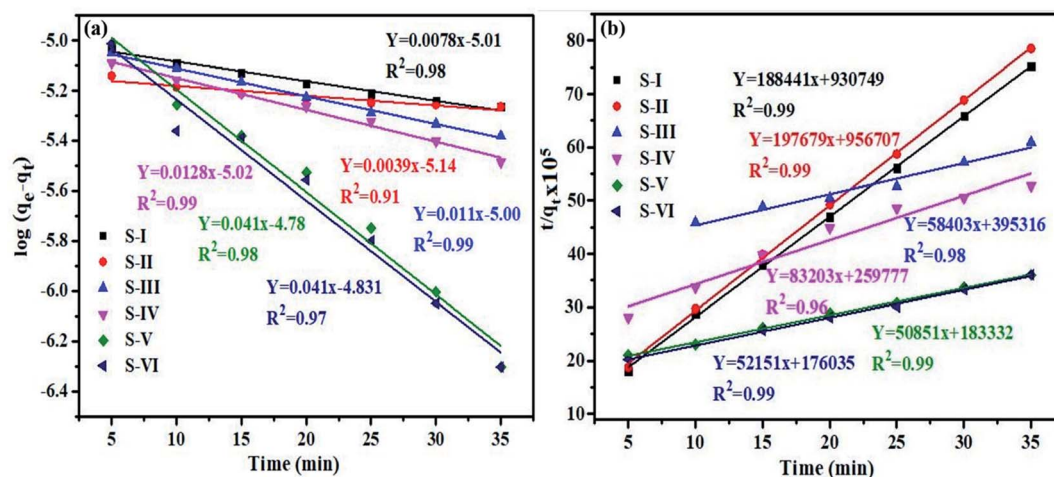| Semiconductor/ heterojunction	First order		Second order	
	K_1	R^2	K_2	R^2
S-I	0.063	0.98	3.2×10^3	0.89
S-II	0.045	0.98	11.3×10^3	0.98
S-III	0.096	0.98	4.6×10^3	0.93
S-IV	0.183	0.99	3.0×10^3	0.91
S-V	0.283	0.98	28.3×10^3	0.99
S-VI	0.374	0.97	2.9×10^3	0.86

Fig. 10   Graph (a) pseudo first and (b) second order kinetics models for degradation of RhB dye over the $MnV_2O_6/BiVO_4$ heterojunction.

Table 3 Various factors of the kinetic models for degradation of RhB dye

Semiconductor/ heterojunction	First order		Second order	
	K_1	R^2	K_2	R^2
S-I	0.008	0.98	83.2×10^3	0.99
S-II	0.004	0.91	40.8×10^2	0.99
S-III	0.011	0.99	8.6×10^3	0.98
S-IV	0.013	0.99	26.6×10^3	0.96
S-V	0.041	0.98	14.1×10^3	0.99
S-VI	0.041	0.97	15.4×10^3	0.99

products. A comparison of photocatalytic efficiency of some heterojunctions for degradation of organic contaminants is presented in Table 1.

3.4 Photocatalytic degradation kinetics

Furthermore, pseudo first and second order models were used to explore the kinetics of dye degradation. The pseudo first order rate equation of Langmuir is given as: $\log(q_e - q_t) = \log q_e - k_1 t$, where q_e and q_t denote the concentration of dye adsorbed at equilibrium and at any time t, and the first order rate constant is represented by K_1. The plot of $\ln(q_e - q_t)$ $vs.$ t for pseudo first order kinetics of MB dye is shown in Fig. 9a. The calculated values of K_1 and R^2 are given in Table 2.

The pseudo-second order rate equation was also applied to MB dye and is represented as: $t/q_t = 1/K_2(q_e)^2 + t/q_t$, where K_2 is the second order rate constant. Fig. 9b demonstrates the plot of (t/q_t) $vs.$ t for pseudo second order kinetics of MB dye and K_2 and R^2 values are given in Table 2.

A similar process was established for rhodamine B (RhB) for thorough comparison of kinetics. Fig. 10(a and b) presents both the kinetic models for the degradation of RhB dye.

The calculated K_1, K_2 and R^2 values for RhB dye are given in Table 3. Furthermore, the model's applicability is examined using the R^2 values of all photocatalyst samples.

Interestingly, the results of kinetic models for the dyes are different. The R^2 value for MB dye varies from 0.97 to 0.99, and 0.86 to 0.99 for pseudo first and second order kinetic models,
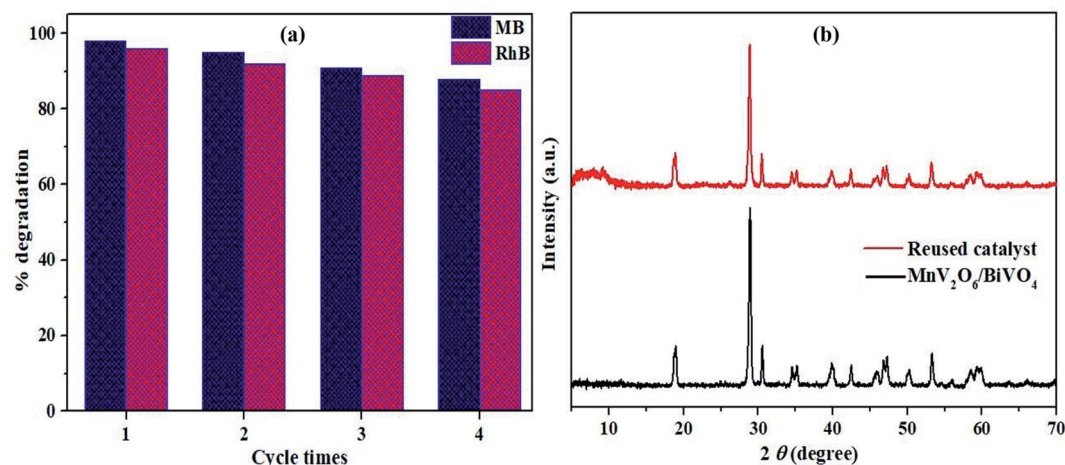

Fig. 11   (a) Reusability of $MnV_2O_6/BiVO_4$ catalyst for MB and RhB dye degradation; (b) XRD pattern of the unutilized and reused catalyst.

respectively. For RhB dye, R^2 varies from 0.91 to 0.99 and 0.96 to 0.99 for first and second order kinetic models, respectively. As a result, the data indicate that photocatalytic degradation of MB dye used a pseudo-first order process, whereas RhB dye used a pseudo-second order mechanism.

The cycling tests were performed to check the stability and reusability of $MnV_2O_6/BiVO_4$ heterojunction (S-V) for photocatalytic degradation of MB and RhB dyes in solar light. The activity of the heterojunction was retained to a significant extent even after four consecutive cycles (Fig. 11a). The crystallinity and crystal structure of the photocatalyst were retained after four consecutive cyclic runs which is supported by the XRD pattern (Fig. 11b). The absence of leaching on the exterior throughout the photocatalytic response might be responsible for the insignificant drop in photocatalytic execution. These results indicate equitable stability and reusability of the synthesized heterojunction with extensive activity.

4. Conclusions

$MnV_2O_6/BiVO_4$ heterojunction samples were prepared employing a hydrothermal technique. Among the synthesized samples, $MnV_2O_6/BiVO_4$ heterojunction sample (S-V) with a ratio of 0.75 : 1.00 ($MnV_2O_6 : BiVO_4$) showed the best performance under direct sunlight exposure for MB and RhB dye degradation. The active species playing the most significant role in dye photodegradation with $MnV_2O_6/BiVO_4$ heterojunction was determined by employing isopropyl alcohol (IPA), potassium iodide (KI) and benzoquinone (BQ) as scavengers for $^\bullet OH$, h^+ and $^\bullet O_2^-$ radicals, respectively. The results revealed that degradation of dyes was significantly suppressed with BQ suggesting that $^\bullet O_2^-$ played a key role in the photocatalytic degradation process. Furthermore, $MnV_2O_6/BiVO_4$ heterojunction also successfully reduced 4-NP into 4-AP in a time span of 40 min without the production of any intermediates. This study provides an easy and speedy process for the degradation of toxic contaminants in waste water using direct sunlight.

Conflicts of interest

There are no conflicts to declare.

References

1 D. Shahidi, R. Roy and A. Azzouz, Advances in catalytic oxidation of organic pollutants – Prospects for thorough mineralization by natural clay catalysts, *Appl. Catal., B*, 2015, **174**, 277–292.

2 A. Chatterjee, S. Shamim, A. K. Jana and J. K. Basu, Insights into the competitive adsorption of pollutants on a mesoporous alumina–silica nanosorbent synthesized from coal fly ash and a waste aluminium foil, *RSC Adv.*, 2020, **10**, 15514–15522.

3 N. Kaur, J. Kaur, R. Badru, S. Kaushal and P. P. Singh, BGO/AlFu MOF core shell nano-composite based bromide ion-selective electrode, *J. Environ. Chem. Eng.*, 2020, **8**, 104375.

4 C. Bradu, M. Magureanu and V. I. Parvulescu, Degradation of the chlorophenoxyacetic herbicide 2,4-D by plasma-ozonation system, *J. Hazard. Mater.*, 2017, **336**, 52–56.

5 M. Bilal and H. M. N. Iqbal, Microbial bioremediation as a robust process to mitigate pollutants of environmental concern, *Case Studies in Chemical and Environmental Engineering*, 2020, **2**, 100011.

6 M. N. Chong, B. Jin, C. W. K. Chow and C. Saint, Recent developments in photocatalytic water treatment technology: a review, *Water Res.*, 2010, **44**, 2997–3027.

7 M. Ni, M. K. H. Leung, D. Y. C. Leung and K. Sumathy, A review and recent developments in photocatalytic water-splitting using TiO_2 for hydrogen production, *Renewable Sustainable Energy Rev.*, 2007, **11**, 401–425.

8 M. Muuronen, S. M. Parker, E. Berardo, A. Le, M. A. Zwijnenburg and F. Furche, Mechanism of Photocatalytic Water Oxidation on Small TiO_2 Nanoparticles, *Chem. Sci.*, 2017, **8**, 2179–2183.

9 F. Lin, Z. Shao, P. Li, Z. Chen, X. Liu, M. Li, B. Zhang, J. Huang, G. Zhu and B. Dong, Low-cost dual cocatalysts $BiVO_4$ for highly efficient visible photocatalytic oxidation, *RSC Adv.*, 2017, **7**, 15053.

10 P. R. Paivaa and T. Noel, Application of Metal Oxide Semiconductors in Light-Driven Organic Transformations, *Catal. Sci. Technol.*, 2019, **9**, 5186–5232.

11 H. Xu, S. Ouyang, L. Liu, P. Reunchan, N. Umezawaace and J. Ye, Recent advances in TiO_2-based photocatalysis, *J. Mater. Chem. A*, 2014, **2**, 12642.

12 X. Shena, H. Shaoc, Y. Liua and Y. Zhai, Synthesis and photocatalytic performance of ZnO with flower-like structure from zinc oxide ore, *J. Mater. Sci. Technol.*, 2020, **51**, 1–7.

13 M. Ganeshbabu, N. Kannan, P. S. Venkatesh, G. Paulraj, K. Jeganathan and D. M. Ali, Synthesis and characterization of $BiVO_4$ nanoparticles for environmental applications, *RSC Adv.*, 2020, **10**, 18315.

14 L. Suna, J. Suna, X. Yang, S. Bai, Y. Feng, R. Luo, D. Li and A. Chen, An integrating photoanode consisting of $BiVO_4$, rGO and LDH for photoelectrochemical water splitting, *Dalton Trans.*, 2019, **48**, 16091–16098.

15 H. Hirakawa, S. Shiota, Y. Shiraishi, H. Sakamoto, S. Ichikawa and T. Hirai, Au Nanoparticles Supported on $BiVO_4$: Effective Inorganic Photocatalysts for H_2O_2 Production from Water and O_2 under Visible Light, *ACS Catal.*, 2016, **6**, 4976–4982.

16 X. Xu, M. Du, T. Chen, S. Xiong, T. Wu, D. Zhao and Z. Fan, New insights into Ag-doped $BiVO_4$ microspheres as visible light photocatalysts, *RSC Adv.*, 2016, **6**, 98788.

17 J. H. Baek, T. M. Gill, H. Abroshan, S. Park, X. Shi, J. Nørskov, H. S. Jung, S. Siahrostami and X. Zheng, Selective and Efficient Gd-Doped $BiVO_4$ Photoanode for Two-Electron Water Oxidation to H_2O_2, *ACS Energy Lett.*, 2019, **4**, 720–728.

18 C. Regmi, T. H. Kim, S. K. Ray, T. Yamaguchi and S. W. Lee, Cobalt-doped $BiVO_4$ (Co-$BiVO_4$) as a visible-lightdriven photocatalyst for the degradation of malachitegreen and inactivation of harmful microorganisms in wastewater, *Res. Chem. Intermed.*, 2017, **43**, 5203–5216.

19 E. A. Ruiz, M. G. Galvan, P. Z. Robledo, J. C. B. Pacheco, J. V. Arenas, J. Peral and U. M. Garcia-Perez, Facile synthesis of visible-light-driven $Cu_2O/BiVO_4$ composites for the photomineralization of recalcitrant pesticides, *RSC Adv.*, 2017, **7**, 45885.

20 J. Zhang, F. Ren, M. Deng and Y. Wang, Enhanced visible-light photocatalytic activity of a $g\text{-}C_3N_4/BiVO_4$ nanocomposite: a first-principles study, *Phys. Chem. Chem. Phys.*, 2015, **17**, 10218.

21 P. Ju, P. Wang, B. Li, H. Fan, S. Ai, D. Zhang and Y. Wang, A novel calcined $Bi_2WO_6/BiVO_4$ heterojunction photocatalyst with highly enhanced photocatalytic activity, *Chem. Eng. J.*, 2014, **236**, 430–437.

22 B. Zoellner, E. Gordon and P. A. Maggard, A small bandgap semiconductor, p-type MnV_2O_6, active for photocatalytic hydrogen and oxygen production, *Dalton Trans.*, 2017, **46**, 10657–10664.

23 S. Kaushal, P. Kurichh, K. Kaur and P. P. Singh, Novel 3D flower like ZnO/MnV_2O_6 heterojunction as an efficient adsorbent for the removal of imidacloprid and photocatalyst for degradation of organic dyes in waste water, *Polyhedron*, 2021, **201**, 115161.

24 M. Nithya, S. Vidhya and K. Praveen, A Novel $g\text{-}C_3N_4/MnV_2O_6$ Heterojunction Photocatalyst for the Removal of Methylene Blue and Indigo Carmine, *Chem. Phys. Lett.*, 2019, **737**, 136832.

25 X. Zhang, X. Lia, F. Jianga, W. Dua, C. Houa, Z. Xua, L. Zhua, Z. Wanga, H. Liua, W. Zhoua and H. Yuan, Improved electrochemical performance of 2D accordion-like MnV_2O_6 nanosheets as anode materials for Li-ion batteries, *Dalton Trans.*, 2020, **49**, 1794–1802.

26 M. Yan, Y. Yan, Y. Wu, W. Shi and Y. Hua, Microwave-assisted synthesis of monoclinic–tetragonal $BiVO_4$ heterojunctions with enhanced visible-light-driven photocatalytic degradation of Tetracycline, *RSC Adv.*, 2015, **5**, 90255.

27 F. Guo, W. Shi, X. Lin and G. Che, Hydrothermal synthesis of graphitic carbon nitride–$BiVO_4$ composites with enhanced visible light photocatalytic activities and the mechanism study, *J. Phys. Chem. Solids*, 2014, **75**, 1217–1222.

28 Y. Singh, S. Kaushal and R. S. Sodhi, Biogenic synthesis of silver nanoparticles using cyanobacterium Leptolyngbya sp. WUC 59 cell-free extract and their effects on bacterial growth and seed germination, *Nanoscale Adv.*, 2020, **2**, 3972–3982.

29 S. V. Kite, D. J. Sathe, A. N. Kadam, S. S. Chavan and K. M. Garadkar, Highly efficient photodegradation of 4-nitrophenol over the nano-TiO_2 obtained from chemical bath deposition technique, *Res. Chem. Intermed.*, 2020, **46**, 1255–1282.

30 S. Kaushal, N. Kaur, M. Kaur and P. P. Singh, Dual-responsive pectin/graphene oxide (Pc/GO) nano-composite as an efficient adsorbent for $Cr(III)$ ions and photocatalyst for degradation of organic dyes in waste water, *J. Photochem. Photobiol., A*, 2020, **403**, 112841.

31 T. Palaniselvam, L. Shi, G. Mettela, D. H. Anjum, R. Li, K. P. Katuri, P. E. Saikaly and P. Wang, Vastly Enhanced $BiVO_4$ Photocatalytic OER Performance by $NiCoO_2$ as Cocatalyst, *Adv. Mater. Interfaces*, 2017, **4**, 1700540.

32 M. Long, W. Cai, J. Cai, B. Zhou, X. Chai and Y. Wu, Efficient Photocatalytic Degradation of Phenol over $Co_3O_4/BiVO_4$ Composite under Visible Light Irradiation, *J. Phys. Chem. B*, 2006, **110**, 20211–20216.

33 Z. Zhang, M. Wang, W. Cui and H. Sui, Synthesis and characterization of a core–shell $BiVO_4@g\text{-}C_3N_4$ photocatalyst with enhanced photocatalytic activity under visible light irradiation, *RSC Adv.*, 2017, **7**, 8167–8177.

34 M. Guo, Y. Wang, Q. He, W. Wang, W. Wang, Z. Fu and H. Wang, Enhanced photocatalytic activity of S-doped $BiVO_4$ photocatalysts, *RSC Adv.*, 2015, **5**, 58633.

35 X. Lin, L. Yu, L. Yan, H. Li, Y. Yan, C. Liu and H. Zhai, Visible light photocatalytic activity of $BiVO_4$ particles with different Morphologies, *Solid State Sci.*, 2014, **32**, 61–66.

36 E. Abroushan, S. Farhadi and A. Zabardasti, $Ag_3PO_4/CoFe_2O_4$ magnetic nanocomposite: synthesis, characterization and applications in catalytic reduction of nitrophenols and sunlight-assisted photocatalytic degradation of organic dye pollutants, *RSC Adv.*, 2017, **7**, 18293–18304.

37 A. H. Abbar, A. H. Sulaymon and M. G. Jalhoom, Scale-up of a fixed bed electrochemical reactor consisting of parallel screen electrode used for p-aminophenol production, *Electrochim. Acta*, 2007, **53**, 1671–1679.

38 M. Nasrollahzadeh, S. M. Sajadi, A. R. Vartooni, M. Alizadeh and M. Bagherzadeh, Green synthesis of the Pd nanoparticles supported on reduced graphene oxide using barberry fruit extract and its application as a recyclable and heterogeneous catalyst for the reduction of nitroarenes, *J. Colloid Interface Sci.*, 2016, **466**, 360–368.

39 Y. Liu, H. Xu and H. Yu, Synthesis of lignin-derived nitrogen-doped carbon as a novel catalyst for 4-NP reduction evaluation, *Sci. Rep.*, 2020, **10**, 20075.

40 K. Yu, S. Yang, C. Liu, H. Chen, H. Li, C. Sun and S. A. Boyd, Degradation of Organic Dyes via Bismuth Silver Oxide Initiated Direct Oxidation Coupled with Sodium Bismuthate Based Visible Light Photocatalysis, *Environ. Sci. Technol.*, 2012, **46**, 7318–7326.

41 Y. Ghaffari, N. K. Gupta, J. Bae and K. S. Kim, One-step fabrication of Fe_2O_3/Mn_2O_3 nanocomposite for rapid photodegradation of organic dyes at neutral pH, *J. Mol. Liq.*, 2020, **315**, 113691.

42 M. Mousavi, A. H. Yangjeh and M. Abitorabi, Fabrication of novel magnetically separable nanocomposites using graphitic carbon nitride, silver phosphate and silver chloride and their applications in photocatalytic removal of different pollutants using visible-light irradiation, *J. Colloid Interface Sci.*, 2016, **480**, 218–231.

43 S. R. Morrison, *Electrochemistry at Semiconductor and Oxidized Metal Electrode*, Plenum, New York, 1980.

44 Q. Yuan, L. Chen, M. Xiong, J. He, S. L. Luo, C. T. Au and S. F. Yin, $Cu_2O/BiVO_4$ heterostructures: synthesis and application in simultaneous photocatalytic oxidation of organic dyes and reduction of $Cr(VI)$ under visible light, *Chem. Eng. J.*, 2014, **255**, 394–402.

45 M. Han, T. Sun, P. Y. Tan, X. Chen, O. K. Tan and M. S. Tse, m-BiVO$_4$@γ-Bi$_2$O$_3$ core–shell p–n heterogeneous nanostructure for enhanced visible-light photocatalytic performance, *RSC Adv.*, 2013, **3**, 24964–24970.

46 Parul, K. Kaur, R. Badru, P. Singh and S. Kaushal, Photodegradation of organic pollutants using heterojunctions: A review, *J. Environ. Chem. Eng.*, 2020, **8**, 103666.

47 S. Ma, J. Xue, Y. Zhou and Z. Zhang, Photochemical synthesis of ZnO/Ag$_2$O heterostructures with enhanced ultraviolet and visible photocatalytic activity, *J. Mater. Chem. A*, 2014, **2**, 7272.

48 D. Wang, L. Guo, Y. Zhen, L. Yue, G. Xue and F. Fu, AgBr quantum dots decorated mesoporous Bi$_2$WO$_6$ architectures with enhanced photocatalytic activities for methylene blue, *J. Mater. Chem. A*, 2014, **2**, 11716–11727.

49 O. A. Zelekew and D. H. Kuo, A two-oxide nanodiode system made of double-layered p-type Ag$_2$O@n-type TiO$_2$ for rapid reduction of 4-nitrophenol, *Phys. Chem. Chem. Phys.*, 2016, **18**, 4405.

50 F. Y. Tian, D. Hou, W. M. Zhang, X. Q. Qiao and D. S. Li, Synthesis of Ni$_2$P/Ni$_{12}$P$_5$ bi-phase nanocomposite for efficient catalytic reduction of 4-nitrophenol based on the unique n-n heterojunction effects, *Dalton Trans.*, 2017, **46**, 14107–14113.

51 Y. T. Prabhu, V. N. Rao, M. V. Shankar, B. Sreedhar and U. Pal, Facile hydrothermal synthesis of CuO@ZnO heterojunction nanostructures for enhanced photocatalytic hydrogen evolution, *New J. Chem.*, 2019, **43**, 6794–6805.

52 A. S. Kshirsagar and P. K. Khanna, CuSbSe$_2$/TiO$_2$: novel type-II heterojunction nano-photocatalyst, *Mater. Chem. Front.*, 2019, **3**, 437–449.

53 A. Verma, D. P. Jaihindh and Y. P. Fu, Photocatalytic 4-nitrophenol degradation and oxygen evolution reaction in CuO/g-C$_3$N$_4$ composites prepared by deep eutectic solvent assisted chlorine Doping, *Dalton Trans.*, 2019, **48**, 8594–8610.

54 A. Verma, S. Kumar, W. K. Chang and Y. P. Fu, Bi-functional Ag-Cu$_x$O/g-C$_3$N$_4$ hybrid catalysts for the reduction of 4-nitrophenol and the electrochemical detection of dopamine, *Dalton Trans.*, 2020, **49**, 625–637.

55 M. M. Sabzehmeidani, H. Karimi and M. Ghaedi, Enhanced visible light-active CeO$_2$/CuO/Ag$_2$CrO$_4$ ternary heterostructures based on CeO$_2$/CuO nanofiber heterojunctions for the simultaneous degradation of a binary mixture of dyes, *New J. Chem.*, 2020, **44**, 5033–5048.

56 V. Jayaraman, C. Ayappan, B. Palanivel and A. Mani, Bridging and synergistic effect of the pyrochlore like Bi$_2$Zr$_2$O$_7$ structure with robust CdCuS solid solution for durable photocatalytic removal of the organic pollutants, *RSC Adv.*, 2020, **10**, 8880.

57 Q. Wang, B. Li, P. Zhang, W. Zhang, X. Hua and X. Li, 2D black phosphorus and tungsten trioxide heterojunction for enhancing photocatalytic performance in visible light, *RSC Adv.*, 2020, **10**, 27538.

58 T. Zeng, D. Shi, Q. Cheng, G. Liao, H. Zhou and Z. Pan, Constructing of novel phosphonate-based MOF/P-TiO$_2$ Heterojunction Photocatalysts: enhanced photocatalytic performance and mechanistic insight, *Environ. Sci.: Nano*, 2020, **7**, 861–879.